The Astrophysical Journal, 746:45 (16pp), 2012 February 10 doi:10.1088/0004-637X/746/1/45

CHARACTERIZING THE ATMOSPHERES OF TRANSITING PLANETS WITH A DEDICATED SPACE TELESCOPE

M. Tessenyi[1,2], M. Ollivier[3,4], G. Tinetti[1], J. P. Beaulieu[2], V. Coudé du Foresto[5], T. Encrenaz[5], G. Micela[6], B. Swinyard[1,7], I. Ribas[8], A. Aylward[1], J. Tennyson[1], M. R. Swain[9], A. Sozzetti[10], G. Vasisht[9], and P. Deroo[9]
[1] Department of Physics and Astronomy, University College London, Gower Street, London WC1E 6BT, UK
[2] Institut d'Astrophysique de Paris, CNRS, UMR7095, Université Paris VI, 98bis Boulevard Arago, Paris, France
[3] Institut d'Astrophysique Spatiale, Université de Paris-Sud and CNRS (UMR 8617), IAS UMR8617, Orsay F-91405, France
[4] CNRS, Orsay F-91405, France
[5] Observatoire de Paris, LESIA, Meudon, France
[6] INAF-Osservatorio Astronomico di Palermo, Piazza del Parlamento 1, 90134 Palermo, Italy
[7] RAL Space, STFC-Rutherford Appleton Laboratory, Harwell Campus, Chilton, Didcot, Oxon OX11 0QX, UK
[8] Institut de Ciencies de l'Espai (CSIC-IEEC), Campus UAB, 08193 Bellaterra, Spain
[9] Jet Propulsion Laboratory, California Institute of Technology, 4800 Oak Grove Drive, Pasadena, CA 91109-8099, USA
[10] INAF-Osservatorio Astronomico di Torino, Strada Osservatorio 20, 10025 Pino Torinese (TO), Italy
Received 2011 June 13; accepted 2011 November 1; published 2012 January 24

ABSTRACT

Exoplanetary science is one of the fastest evolving fields of today's astronomical research, continuously yielding unexpected and surprising results. Ground-based planet-hunting surveys, together with dedicated space missions such as *Kepler* and *CoRoT*, are delivering an ever-increasing number of exoplanets, over 690, and ESA's *Gaia* mission will escalate the exoplanetary census into the several thousands. The next logical step is the characterization of these new worlds. What is their nature? Why are they as they are? Use of the *Hubble Space Telescope* and *Spitzer Space Telescope* to probe the atmospheres of transiting hot, gaseous exoplanets has opened perspectives unimaginable even just 10 years ago, demonstrating that it is indeed possible with current technology to address the ambitious goal of characterizing the atmospheres of these alien worlds. However, these successful measurements have also shown the difficulty of understanding the physics and chemistry of these exotic environments when having to rely on a limited number of observations performed on a handful of objects. To progress substantially in this field, a dedicated facility for exoplanet characterization, able to observe a statistically significant number of planets over time and a broad spectral range will be essential. Additionally, the instrument design (e.g., detector performances, photometric stability) will be tailored to optimize the extraction of the astrophysical signal. In this paper, we analyze the performance and tradeoffs of a 1.2/1.4 m space telescope for exoplanet transit spectroscopy from the visible to the mid-IR. We present the signal-to-noise ratio as a function of integration time and stellar magnitude/spectral type for the acquisition of spectra of planetary atmospheres for a variety of scenarios: hot, warm, and temperate planets orbiting stars ranging in spectral type from hot F- to cooler M-dwarfs. Our results include key examples of known planets (e.g., HD 189733b, GJ 436b, GJ 1214b, and Cancri 55 e) and simulations of plausible terrestrial and gaseous planets, with a variety of thermodynamical conditions. We conclude that even most challenging targets, such as super-Earths in the habitable zone of late-type stars, are within reach of an M-class, space-based spectroscopy mission.

Key words: infrared: planetary systems – planets and satellites: atmospheres – stars: late-type – stars: low-mass

Online-only material: color figures

1. INTRODUCTION

The science of extrasolar planets is one of the most rapidly changing areas of astrophysics, and since 1995 the number of known planets has increased by almost two orders of magnitude. A combination of ground-based surveys and dedicated space missions has resulted in over 690 planets being detected (Schneider 2011), and over 1200 that await confirmation (Borucki et al. 2011). NASA's *Kepler* mission has opened up the possibility of discovering Earth-like planets in the habitable zone (HZ) around some of the 100,000 stars it is surveying during its three- to four-year lifetime. The new ESA *Gaia* mission is expected to discover thousands of new planets around stars within 200 pc of the Sun (Casertano et al. 2008; Sozzetti 2010). Meanwhile, transit and combined light methods have allowed the characterization of the atmosphere of a few hot large bodies close to their star using current space telescopes (e.g., Charbonneau et al. 2002; Harrington et al. 2006; Crossfield et al. 2010; Knutson et al. 2007b; Tinetti et al. 2007b, 2010a; Beaulieu et al. 2008, 2010; Swain et al. 2008a, 2008b, 2009b, 2009a; Grillmair et al. 2008; Stevenson et al. 2010) and ground-based telescopes (Redfield et al. 2008; Snellen et al. 2008, 2010; Swain et al. 2010; Waldmann et al. 2012). Transiting hot super-Earths, which are very interesting targets since they are absent from our solar system, are within reach with current telescopes, e.g., GJ 1214b (Charbonneau et al. 2009; Bean et al. 2010), and Cancri 55 e (Winn et al. 2011).

The next generation of ground-based telescopes and the *James Webb Space Telescope* will have a noticeably larger collection area compared to current facilities, allowing them to probe fainter targets in the future. However, these facilities are built for the larger astrophysics community and are not necessarily optimized for exoplanet characterization. The investigation of exoplanetary atmospheres requires a dedicated space mission that is fine-tuned for this purpose. Such a mission should be able to not only simultaneously capture the spectral signatures

Table 1
Subdivision of Planetary Atmospheres According to Temperature and Planetary Size

Temperature/Size	Jupiter-like	Neptune-like	Super-Earth
Hot	**HJ**	HN	**HSE**
Warm	WJ	**WN**	**WSE**
HZ	**HZ-J**	HZ-N	**HZ-SE**

Notes. The difficulty in the observations increases from left to right and from top to bottom. All categories in bold are studied in detail in Section 3; results for the three other categories can be extrapolated.

over a broad wavelength region to reveal the chemical and dynamical processes of the atmosphere, but also have enough time to observe many systems repeatedly. These systems should include the dimmer planets that approach the size of Earth, hence the instrument design should be optimized to eliminate systematic errors.

In this paper, we consider the possibilities offered by—and the tradeoffs of—a 1.2–1.4 m space-based telescope capable of performing spectroscopy from the visible down to the mid-IR. A similar mission concept has most recently been selected for an assessment study by ESA, under the name *Exoplanet Characterisation Observatory* (*EChO*;[11] Tinetti et al. 2011b).

2. METHODS

2.1. Classification of Planetary Atmospheres

We classified the planetary atmospheres according to equilibrium temperatures and sizes into three classes of atmospheric temperatures—"*Hot*" (800–2000 K), "*Warm*" (350–800 K), and "*Habitable*" (250–350 K)—and three types of planetary sizes—*Jupiter-like, Neptune-like*, and *super-Earth* (see Table 1). Planets with "*Cold*" temperatures (200 K or below) are not studied in this paper.

Super-Earths are expected to be between 1 and 10 $M_\oplus$; in this paper we assume a 5 Earth-mass body for our calculations, with a radius of 1.6–1.8 $R_\oplus$ (Grasset et al. 2009). By comparing Earth's cross-section $\sigma_\oplus = \pi \cdot R_\oplus^2$ to those of the super-Earth, Neptune-like, and Jupiter-like planets, we obtain

$$\sigma_{\rm SE} \sim 3\,\sigma_\oplus; \qquad \sigma_N \sim 25\,\sigma_\oplus; \qquad \sigma_J \sim 100\sigma_\oplus. \tag{1}$$

For transit and combined-light observations (transiting and non-transiting planets), the important parameter is the ratio between the planetary and stellar cross-sections, κ, obtainable by measuring the transit depth:

$$\kappa = \sigma_p/\sigma_*. \tag{2}$$

This parameter changes significantly for different planet/star types. In Table 2, we give σ_* for a few key stellar types, along with the cross-section ratio value κ for the three planetary types considered in this paper, expressed as a factor of $\kappa_{\rm Jupiter}$ ($\kappa_{\rm Jup.} \sim 100\sigma_\oplus/\sigma_\odot$). A Jupiter-sized planet orbiting a Sun-like star and a super-Earth orbiting an M4.5-dwarf will both have a similar cross-section ratio $\kappa \sim \kappa_{\rm Jup.}$, observable with small, ground-based telescopes.

[11] http://sci.esa.int/echo/

2.2. Primary Transit Method

A primary transit occurs when a planet passes in front of its parent star with respect to our line of sight. By subtracting the "in-transit" stellar flux from the "out-of-transit," we can measure directly the parameter κ as described in Equation (2), and hence the planetary radius in units of stellar radii. If we repeat the observation of κ at different wavelengths, we can infer the presence or absence of an atmosphere as well as retrieve the main atmospheric components (Seager & Sasselov 2000; Brown et al. 2001). The spectral absorption of the planetary atmosphere, while in transit, is measured from the transmission spectrum obtained. For key examples of planetary cases, we use synthetic models fitting the existing observations or we extrapolate from our knowledge of the planets in the solar system. The models were calculated with the line-by-line radiative transfer code described in Tinetti et al. (2007a, 2011a), with updated line lists from Barber et al. (2006), Yurchenko et al. (2011), Rothman et al. (2010), and Tashkun & Perevalov (2011). For feasibility studies, we also adopt a more heuristic estimate of the atmospheric contribution rather than these detailed simulations. In particular, the amount of light passing through the atmosphere of the planet will cross a small annulus,

$$\frac{2R_p\pi\Delta z}{\pi {R_\star}^2} = \frac{2R_p\Delta z}{{R_\star}^2}, \tag{3}$$

where R_p is the radius of the planet, $R_\star$ is the radius of the star, and Δz is the height of the atmosphere. From observations, $\Delta z = nH$, where typically $n \sim 5$, depending on the spectral resolution and wavelength. H is the scale height defined by

$$H = \frac{k\,T}{\mu g}, \tag{4}$$

where k is the Boltzmann constant, g is the gravity acceleration, and μ is the mean molecular mass of the atmosphere.

From the scale height expression (4), it is clear that the hotter and lighter the atmosphere is, the easier it is to observe with this technique. Also, dense objects such as telluric bodies will have a higher value for g and consequently a more compact atmosphere. For example, hot Jupiters have high temperatures, low mean molecular mass of the atmosphere ($\mu \sim 2$ amu for hydrogen-rich atmospheres), and relatively low density. Their scale height can easily reach 500 km. By contrast, Earth's temperature is colder (~280 K), μ is ~28 amu, and the bulk composition is denser. As a result, the scale height is compacted to ~8 km.

As explained in Section 2.1, here we are interested in three main classes of planets: gas giants, Neptune-like planets, and super-Earths. While gas giants and Neptunes are optimal targets for primary transit observations, in general super-Earths are the least favorable unless they transit an M star and host a relatively hot and light atmosphere (see Table 3). For this reason, in the most general case, super-Earths should be observed with the secondary eclipse technique, as described in the next section.

2.3. Secondary Eclipse Method

A complementary technique to the primary transit is the so-called secondary eclipse. This method relies on the possibility of observing the star alone when the planet is passing behind it, so we can effectively subtract the stellar contribution from the star+planet system. In practice, we measure the flux emitted

Table 2
Cross-section $\sigma_* = \pi R_*^2$ for Different Stellar Types and Corresponding κ Values for the Three Planet Sizes Considered: Jupiter-like, Neptune-like, and Super-Earth

Star Type	Temperature (K)	Radius ($R_\odot$)	σ_* ($\sigma_\odot$)	$\kappa_{\rm Jup.}$ (κ_J)	$\kappa_{\rm Nept.}$ (κ_J)	$\kappa_{\rm SE}$ (κ_J)
F3V	6740 K	1.56	$\sigma_{F3} \sim 2.4$	~0.5	~0.05	~0.01
G2V	5800 K	1	$\sigma_G = \sigma_\odot$	1	~0.1	~0.02
K1V	4980 K	0.8	$\sigma_{K1} \sim 0.6$	~2	~0.2	~0.03
M1.5V	3582 K	0.42	$\sigma_{M1.5} \sim 0.18$	~6	~0.7	~0.1
M3.5V	3376 K	0.26	$\sigma_{M3.5} \sim 0.07$	~15	~2	~0.3
M4.5V	3151 K	0.17	$\sigma_{M4.5} \sim 0.03$	~35	~4	~0.7
M6V	2812 K	0.12	$\sigma_{M6} \sim 0.01$	~70	~9	~2

Notes. The reader can note that super-Earths in the orbit of late M stars have a similar ratio κ to a Jupiter in the orbit of a Sun-like star.

Table 3
Primary/Secondary Eclipse Flux Ratio for Key Examples of the Planetary Classes Listed in Table 1

Star	Jupiter (K)	Neptune M2.5V	Super-Earth M4V
Hot	0.18	0.98	0.3/0.09
Warm	0.42	2.17	0.7/0.2
HZ	0.9	10.4	1.2/0.3

Notes. Numbers > 1 indicate that the primary transit is more favorable than the secondary, while numbers < 1 indicate the opposite. The results are obtained by dividing the atmospheric signals calculated from Equations (3) and (5), taken at $\sim 10\,\mu$m for all presented cases. For the super-Earth we report two values: a case of an "ocean planet" (1.8 $R_\oplus$; Grasset et al. 2009) with water vapor being the main component of the planetary atmosphere, and a telluric planet with CO_2 as the main atmospheric component (1.6 $R_\oplus$). In the habitable zone, the ratio for the latter case is less favorable, with 0.3 excluding the possibility of primary transit studies. By contrast, for an "ocean planet," the ratio of 1.2 is similar to the ratio for the habitable-zone Jupiter-like planet.

and/or reflected by the planet in units of stellar flux,

$$F_{\rm II}(\lambda) = \left(\frac{R_p}{R_\star}\right)^2 \frac{F_p(\lambda)}{F_\star(\lambda)} = \kappa\, \frac{F_p(\lambda)}{F_\star(\lambda)}, \quad (5)$$

where F_p and $F_\star$ are the planetary and stellar spectra and κ is as defined in Section 2.1. It is clear from this equation that both the relative size of the planet/star (the parameter κ) and the relative temperature are key parameters for secondary eclipse measurements. Here we use synthetic models to represent key examples of exoplanets (Tinetti et al. 2010b). The emitted/reflected spectra were generated with the line-by-line radiative transfer codes described in Tinetti et al. (2005, 2006), with updated line lists from Barber et al. (2006), Yurchenko et al. (2011), and Rothman et al. (2010). For these key cases, the stellar spectra are either observed or modeled (Kurucz 1995). In Figure 1 we show how $F_{\rm II}(\lambda)$ changes for a given planet as a function of star type. In this example, we chose a super-Earth with an Earth-like atmosphere orbiting a selection of known M-dwarfs: clearly, late M stars offer the best planet/star contrast.

Infrared observations. For feasibility studies in the IR, we approximate the planetary and stellar spectra in Equation (5) with two Planck curves at temperatures T_p and $T_\star$, with T_p being the day-side temperature of the planet. While this approximation is not accurate enough to model specific examples, it is helpful when estimating the general case:

$$F_{\rm II}(\lambda) \sim \kappa\, \frac{B_p(\lambda, T_p)}{B_\star(\lambda, T_\star)}. \quad (6)$$

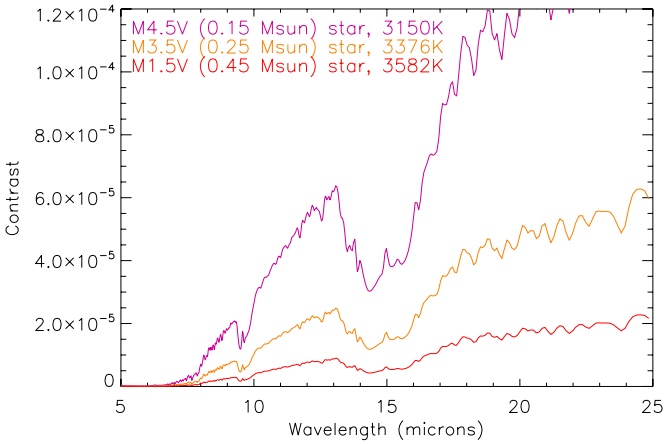

Figure 1. Planet/star flux contrast (Equation (5)) for a super-Earth orbiting different M-type stars (M1.5V, M3.5V, and M4.5V). In this example, the super-Earth is assumed to have an Earth-like atmosphere (see Section 3.3).
(A color version of this figure is available in the online journal.)

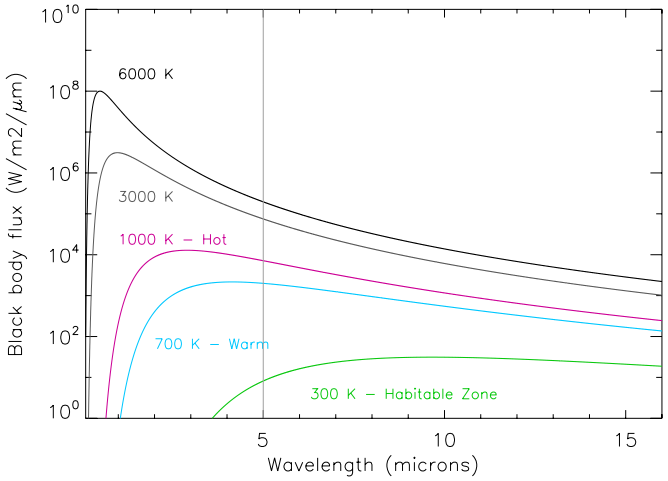

Figure 2. Blackbody curves for effective temperatures of 6000, 3000, 1000, 700, and 300 K. The radiation emitted by the 300 K body is negligible at λ shorter than 5 μm.
(A color version of this figure is available in the online journal.)

In Figure 2, we show the Planck curves for a few bodies at different temperatures. The planet-to-star flux contrast will clearly be higher for hot planets. Note that in the IR temperate planets at ~300 K can be observed only at wavelengths longer than 5 μm, as they emit a negligible amount of flux at $\lambda \leqslant 5\,\mu$m (Figure 2).

Optical observations. For observations in the optical, we need to estimate the reflected light from the planet. Equation (5) becomes

$$F_{\rm II}(\lambda) = \left(\frac{R_p}{R_\star}\right)^2 \frac{F_p(\lambda)}{F_\star(\lambda)} = \kappa\, A\, \zeta\, \frac{R_*^2}{a^2}\, \frac{F_\star(\lambda)}{F_\star(\lambda)} = \kappa\, A\, \zeta\, \frac{R_*^2}{a^2}, \quad (7)$$

where A is the planetary albedo, ζ is the observed fraction of the planet illuminated, and a is the semimajor axis. The closer the planet is to its stellar companion and the higher its albedo, the larger the contrast in the optical will be. For planets colder than ∼1200 K, the reflected light component is predominant in the optical wavelength range ($\lambda < 0.8\,\mu$m). For hotter planets, both Equations (6) and (7) will have a contribution (emission and reflection).

Planet phase variations and eclipse mapping. Phase variations are important to understanding a planet's atmospheric dynamics and the redistribution of absorbed stellar energy from their irradiated day side to the night side. These observations can only be conducted from space since the typical timescale of these phase variations largely exceeds that of one observing night. Phase variations are very insightful both at reflected and thermal wavebands. In the infrared case, these kinds of observations are critical for constraining the General Circulation Models (GCMs) of exoplanets, and of hot gaseous planets in particular. For instance, the infrared 8 μm *Spitzer* observations of the exoplanet HD 189733b have shown the night side of this hot Jupiter to be only ∼300 K cooler than its day side (Knutson et al. 2007a), suggesting an efficient redistribution of the absorbed stellar energy. In addition, toward the optical wavelength regime, an increasing contribution from reflected light is expected (Snellen et al. 2009; Borucki et al. 2009).

A great advantage of a dedicated exoplanet mission would be the potential for long campaigns: staring at a known planetary system for a sizable fraction of an orbit (Knutson et al. 2007a, 2009b, 2009a) or for an entire orbit (Snellen et al. 2009; Borucki et al. 2009), or—provided the flux calibration is accurate enough—using multi-epoch observations to obtain a more sparsely sampled phase curve (Cowan et al. 2007; Crossfield et al. 2010). At thermal wavelengths this may only be interesting for short-period planets, where the diurnal temperature contrast is high. Additionally, non-transiting planets open up interesting possibilities for studying seasons (e.g., Gaidos & Williams 2004). Furthermore, the simultaneous multi-band coverage would make it possible to simultaneously probe the longitudinal temperature distribution as a function of pressure, which would be a very helpful constraint for GCMs.

The potential for using phase variations to study non-transiting systems should also be noted (Selsis et al. 2011). Non-transiting systems will be closer on average than their transiting counterparts. The challenge is stellar and telescope stability over the orbital time of a planet. For planets on circular orbits, thermal phases have limited value because of the inherent degeneracies of inverting phase variations (Cowan & Agol 2008), but for eccentric planets, phase variations will be much richer (Langton & Laughlin 2008; Lewis et al. 2010; Iro & Deming 2010; Cowan & Agol 2011). As one considers increasingly long-period planets (warm rather than hot) even more of them will be on eccentric orbits because of the weaker tidal influence of the host star.

For the brightest targets, eclipses can also be used as powerful tools to spatially resolve the emission properties of planets. During ingress and egress, partial occultation effectively maps the photospheric emission region of the object being eclipsed (Williams et al. 2006; Rauscher et al. 2007; Agol et al. 2010). Key constraints can be placed on three-dimensional atmospheric models through repeated infrared measurements. In this paper, we will focus on the feasibility of primary transits and secondary eclipses. A more detailed and thorough study of the observability of phase variations and eclipse mapping will be the topic of future publications.

2.4. Comparison between Primary and Secondary Transit Techniques

The primary and secondary transit techniques are complementary. Transmission spectra in the infrared, from primary transits, are more sensitive to atomic and molecular abundances, but less to temperature gradients. By comparison, emission spectroscopy allows for detection of molecular species as well as constraining the bulk temperature and vertical thermal gradient of the planet. Additionally, during the primary transit we can sound the terminator, whereas during the secondary eclipse we can observe the planetary day side.

In Table 3, we present ratios of signal values from primary transit and secondary eclipse observations for the key examples of the planetary classes (see Table 1). Given that long integration times require the co-adding of multiple transit observations, for the primary case, any systematic difference in the stellar flux could hamper results. For example, spot redistributions over the stellar surface could potentially alter the depth of the transit, and could be a cause for concern for late-type stars since, on average, they can be quite active. In the case of M-type star super-Earths, though, we rely mostly on secondary eclipse observations which are quite immune from effects related to stellar activity, as the planetary signal follows directly from the depth of the occultation without the need to model the stellar surface.

2.5. Planets Orbiting M-type Stars

In this section, we focus our attention on M-class stars and their HZs. The main reasons to consider them are the following:

1. Among the stars in the solar neighborhood, 90% are M-type (e.g., Perryman & ESA 1997).
2. The relatively small size of M stars (typically between 0.08 and 0.5 $R_\odot$) allows us to probe planetary sizes down to a few Earth masses (see Equation (5)).
3. The low effective temperature of the star ($2900 < T_{\rm eff} < 3900$ K) places the HZ region closer the star than would be the case for a hotter star. An HZ planet will hence have a short orbital period (see Figure 4) and a larger number of transit events will be observable within a given time interval than would be the case for a planet in the HZ of a hotter (K, G, or F) star.
4. M stars are brightest in the IR (i.e., more photons impinging onto the detector), where temperate exoplanets are easier to observe (see Figure 2).

The combination of these effects brings the prospect of characterizing terrestrial planets in the HZs of main-sequence stars within current technology capabilities. By contrast, it is currently impractical to use the transit technique to observe the atmosphere of terrestrial planets in the HZs of more massive stars, as the orbital periods in these cases would be very long (e.g., more than 100 days for a K-type star and 300 for a G-type star). In addition, M-dwarf spectra differ significantly from blackbody radiation curves in the visible and near-infrared

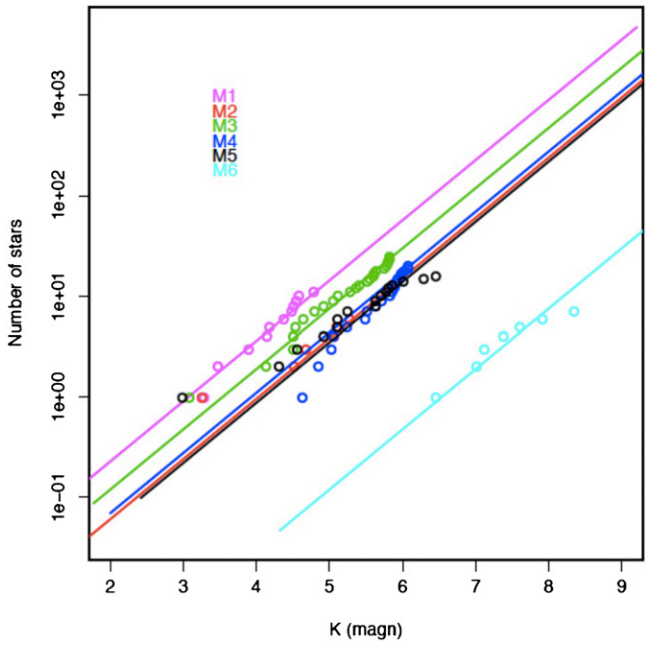

Figure 3. Expected number of stars out to 10 pc, for M0–4V and M5–M9V. Dots are stars in K magnitude from the RECONS catalog and lines represent the expectations, assuming uniform spatial distribution and completeness at 6.6 pc. These plots suggest that the RECONS catalog is complete only up to 6.6 pc for the earliest spectral types and up to 4.5–6 pc for the M5–6V sample. There are too few objects in the M7–9V range to say anything about the completeness/space density of such objects.

(A color version of this figure is available in the online journal.)

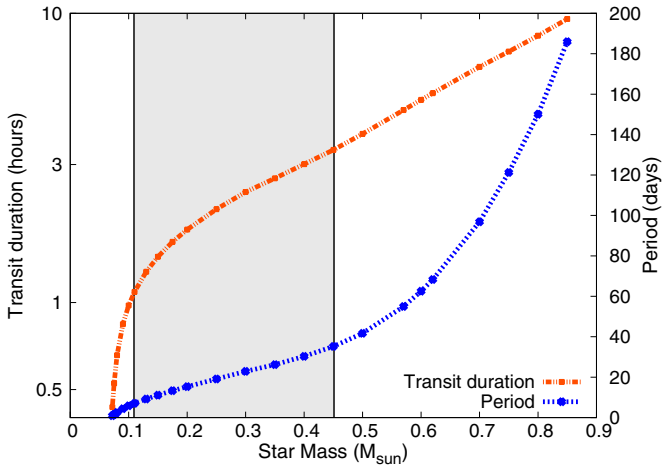

Figure 4. Transit durations and orbital periods of habitable-zone (HZ) super-Earths for varying masses of M stars. Our focus for the HZ is in the mass range delimited by the gray rectangle—between 0.11 and 0.45 $M_{\odot}$, with orbital periods of 7–35 days—and are optimal targets, as seen in Section 2.5. For consistency, we use the same stellar types for hot and warm super-Earths. In these cases, the transit and period durations will clearly be shorter (see Tables 6 and 10 for respective ranges).

(A color version of this figure is available in the online journal.)

parts of the spectrum, but in the mid-infrared, which is considered for our HZ targets, the molecular absorptions are less important.

2.5.1. M-star Population

At the time of this writing, over 25% of stars in the Sun's near neighborhood were believed to be missing from star surveys (such as the catalog by Lépine & Gaidos 2011), in part because bright M stars in the infrared are quite faint in the visible, due to a combination of temperature and the presence of molecular and atomic species absorbing in this spectral region. For instance, an M3V star with $V = 12.30$ mag corresponds to $K = 7.53$ mag, and an M5V star with $V = 15.01$ mag corresponds to $K = 8.40$ mag (Delfosse et al. 2000). For this reason, in this paper we use K magnitude rather than V magnitude to classify the luminosity of M stars. The most complete catalog of late-type nearby stars available today is the Lépine & Gaidos (2011) catalog, which includes nearly 9000 M-dwarfs with magnitude $J < 10$. According to the authors, the catalog represents ∼75% of the estimated ∼11,900 M-dwarfs with $J < 10$ expected to populate the entire sky.

An evaluation of the number of M stars in a magnitude-limited sample can also be derived from the analysis of the 100 nearest RECONS star systems (RECONS 2011). Their distribution in distance shows clearly that, while the M1–4V star sample is evenly distributed within 6.7 pc, the M5–8V sample is significantly incomplete beyond 4–5 pc (see Figure 3). This analysis supports the hypothesis that a significant number of stars are still missing in catalogs in the very close solar neighborhood; there needs to be a major effort in the next years in this direction.

Independent estimates of the M star population in the solar neighborhood were provided by G. Micela (2011, private communication) through color–color diagrams applied to the Two Micron All Sky Survey (2MASS) catalog. This selection might have some contamination from two different sources: (1) distant giant stars may overlap with the nearby very early M type, where the main sequence and giant models are still close together and (2) stars of early spectral type could contaminate the dwarf M-star regime only if highly reddened by intervening dust.

NASA's *WISE* might help to remove the contamination by providing a survey in four additional IR channels (Wright et al. 2010).

The *Gaia* mission, in its all-sky astrometric survey, will deliver direct parallax estimates and spectrophotometry for nearby main-sequence stars down to $R \sim 20$. At the magnitude limit of the survey, distances to relatively bright M stars out to 20–30 pc will be known with 0.1%–1% precision (depending on spectral sub-type). This will constitute an improvement of up to over a factor of 100 with respect to the typical 25%–30% uncertainties in the distance reported for low-mass stars identified as nearby based on proper motion and color selections (e.g., Lépine & Gaidos 2011). Starting with early data releases around mid-mission, *Gaia*'s extremely precise distance estimates, and thus absolute luminosities, to nearby late-type stars will allow us to significantly improve standard stellar evolution models at the bottom of the main sequence. For transiting planet systems, updated values of the masses and radii of the host stars will be of critical importance. Model predictions for the radii of M-dwarfs show typical discrepancies of ∼15% with respect to observations, and, as shown by the GJ 1214b example (Charbonneau et al. 2009), limits in the knowledge of the stellar properties significantly hamper the understanding of the relevant physical characteristics (density, and thus internal structure and composition) of the detected planets. Meanwhile, to account for the possibility of errors in current measurements, we provide a variety of stellar temperatures and calculated corresponding star radii with our results. The radii were calculated using isochrones of old (∼5 Gyr) low-mass stars (Baraffe et al. 1998) and observational constraints (Delfosse et al. 2000). For comparison,

based on the simple radius–temperature–luminosity relation considerations, we can infer that estimates of stellar radii, when *Gaia* parallaxes known to <1% will become available for nearby red stars, will carry much reduced uncertainties, on the order of 1%–3%. Indeed, the precision in the M-dwarf effective temperature estimates from spectroscopy or photometric calibrations (currently, 3%–5% at best) will then become the limiting factor in the knowledge of this fundamental quantity.

2.5.2. Planetary Periods

Figure 4 shows periods and transit durations for HZ super-Earths orbiting a range of M stars. These values clearly depend on orbital distances that are computed by fixing the planet temperature and stellar type. We define the radiation in and out of the planet (in Watts):

$$\mathrm{Rad_{in}} = \pi R_{pl}^2 L_* f(1-A) \tag{8}$$

$$\mathrm{Rad_{out}} = 4\pi R_{pl}^2 \sigma T_{pl}^4, \tag{9}$$

where the planetary albedo is $A = 0.3$, and a small greenhouse effect contribution of $\epsilon = 0.7$ is assumed. The distance of the HZ for each M star type was estimated by considering an average surface temperature for the planet $T_{pl} = 287$ K. More specifically, we started with the bolometric luminosity of the star at a distance a (semimajor axis): $L_* = (4\pi R_*^2 \sigma T_*^4)/(4\pi a^2)$. By equating the radiation in and out of the planet, we obtain an expression for the planetary effective temperature:

$$T_{\mathrm{pl}} = T_* \left(\sqrt{\frac{(1-A)}{\epsilon}} \frac{R_*}{2a} \right)^{1/2}. \tag{10}$$

By imposing $T_{pl} = 287$ K and assuming different values for the stellar temperature, $2900\,\mathrm{K} < T_* < 3900\,\mathrm{K}$, we rearrange this equation to calculate the semimajor axis a and the planetary period $P = 2\pi\sqrt{(a^3/GM)}$. For the other cases presented in this paper, period and transit durations were obtained either using similar calculations, or from observations. For the transit duration t_t we assume a circular, edge-on orbit. From Seager & Mellen-Ornelas (2003) we obtain

$$t_t = \frac{P R_*}{\pi a} \sqrt{\left(1 + \frac{R_{pl}}{R_*}\right)^2 - b^2}. \tag{11}$$

For the general case the impact parameter b was set to zero, unless otherwise specified, so that Equation (11) simplifies to

$$t_t = \frac{P}{\pi} \left(\frac{R_* + R_{pl}}{a} \right). \tag{12}$$

2.6. Estimating the Integration Time

The integration time needed to observe specific targets depends on the following:

1. The parent star: spectral class, type, magnitude in a specified spectral region.
2. The contrast between the parent star and the companion planet in the observed spectral interval: this can be estimated from known observed or simulated objects.
3. The observational requirements: spectral region, resolution, and signal-to-noise ratio (S/N).
4. The telescope characteristics: primary mirror diameter, overall transmission, coverage, and sensitivity of the detectors.
5. The focal plane array characteristics during observation: the number of pixels used per spectral resolution element, readout time, quantum efficiency, full well capacity (FWC), saturation threshold, dark current, and readout noise.

We consider then the flux of photons from the planet. This flux (given in photons/s/m^2 in the whole spectral interval) is converted into electrons/pixel/s/"resolution element" within the defined spectral region using the following expression:

$$F_{e^-} = \frac{F_\gamma \cdot A \cdot \mathrm{transmission} \cdot \mathrm{QE}}{Res \cdot N_{px/\mathrm{Res}}}, \tag{13}$$

where F_{e^-} and F_γ are, respectively, the electron and photon fluxes, A is the telescope mirror surface area, QE is the quantum efficiency, Res is the number of spectral elements in the band (resolution), and $N_{px/\mathrm{Res}}$ is the number of pixels per resolution element. From here on, F will only refer to the electron flux: F_{e^-}. The *transmission* is the overall fraction of energy that reaches the detector (before conversion to electrons). It includes the telescope and instrument (optical) transmission.

Using these values, the time required for one detector pixel readout is computed:

$$t_{\mathrm{ro}} = \frac{\mathrm{FWC} \cdot \mathrm{saturation}}{F_\star + F_{pl} + \mathrm{DC}}, \tag{14}$$

where "ro" stands for read out, FWC for full well capacity, DC for dark current, and *saturation* is a fraction of the FWC. Usually, a saturation at 70% of the FWC is taken into account, that is, the limit of electrons that can be accumulated in a single exposure.

The number of readouts required is then computed using the following formula:

$$N_{\mathrm{ro}} = (\mathrm{S/N})^2 \cdot \frac{F_\star + F_{\mathrm{pl}} + \mathrm{DC} + (\mathrm{RON}^2/t_{\mathrm{ro}})}{F_{\mathrm{pl}}^2 \cdot t_{\mathrm{ro}} \cdot N_{px/\mathrm{Res}}}, \tag{15}$$

where S/N is the signal-to-noise ratio within the defined spectral band and RON is the detector readout noise. For the secondary eclipse case, F_{pl} is the flux emitted or reflected by the planet, while for the primary transit case (explained in Section 2.2), F_{pl} corresponds to the amount of flux (written as a negative) absorbed by the planet's atmosphere,

$$F_{\mathrm{pl}} = -\frac{\pi {R_{\mathrm{pl}}}^2}{\pi {R_\star}^2} \left(\left(1 + \frac{nH^2}{R_{\mathrm{pl}}}\right) - 1 \right) = -\frac{2nH R_{\mathrm{pl}}}{{R_\star}^2}, \tag{16}$$

where n is an atmospheric absorption factor.

With these values, the total integration time is computed by multiplying the duration of a detector pixel readout by the number of readouts required.

The planet/star flux contrast ratio and the star brightness are the obvious main factors affecting integration times. To estimate the contrast, we have considered observed spectra and simulated synthetic spectra of stellar and planetary atmospheres (Sections 2.1–2.5).

2.6.1. Instrument Detector and Validation

Table 4 lists the instrument setting values we have assumed for our simulator to cover the four bands in which our results are given.

Table 4
Instrument Settings Used in Our Simulations, Listed for Each Observing Band Used

Instrument Values	Visible	2.5–5 μm	5–11 μm	11–16 μm
Detector Used (SOFRADIR)	CCD	MWIR	LWIR	VLWIR
Full well capacity (electrons)	2×10^6	4×10^6	2×10^7	5×10^6
Dark current (electrons s^{-1} $pixel^{-1}$)	0.1	10	500	300
Quantum efficiency (electrons $photon^{-1}$)	0.5	0.7	0.7	0.7
Readout noise (electrons $pixel^{-1}$ $readout^{-1}$)	10	400	1000	1000
Readout time (s)	0.004	0.01	0.03	0.01
Telescope temperature (K)	0	60	60	60
Instrument temperature (K)	0	45	45	45
Telescope transmission	0.85	0.9	0.9	0.9
Instrument transmission	0.7	0.7	0.7	0.7

Notes. In addition, the two following settings are the same for all four bands considered: a 30 μm pixel size and 2 illuminated pixels per spectral element are assumed. For the *N* band (7.7–12.7 μm) we have used the LWIR setting values. Note that in the case of the VLWIR detector, we have used a dark current value of 300 electrons s^{-1} $pixel^{-1}$ considering existing technologies and expected future capabilities. Further discussion of these values can be found in Section 4.4. In the Appendix we give two other options, compatible with a 1.2 m telescope, and a different selection of detectors and instrument parameters.

To validate our tool, we have incorporated in our instrument simulator the parameters of *Hubble* NICMOS, and compared our results for hot gaseous planets with observed data from NICMOS. We obtained results in excellent agreement with the observed data.

3. RESULTS

We present our results ordered by planetary temperature: hot, warm, and temperate (habitable zone, HZ). For our key examples we have calculated the flux contrast by using synthetic models (see Sections 2.2 and 2.3), which either fit existing observations or are extrapolated from our knowledge of the solar system planets. For feasibility studies we prefer to adopt cruder estimates of atmospheric contributions (i.e., blackbody curves) rather than detailed simulations of each specific case. Plots of flux contrasts are given for each case, accompanied by integration times represented as "number of transits" (based on transit durations and orbital periods; see Section 2.5.2), with a maximum number of transits indicated. This number is estimated by dividing the nominal lifetime of a mission (we consider five years here) by the orbital period for each target. For each case, integration times are given over a range of stellar magnitudes. The signal-to-noise and resolution (S/N/Res) values vary from table to table, from $R = 300$ to $R = 10$, and S/N = 50 to S/N = 5. For each target, these values were selected to optimize the scientific return across the magnitude range considered. The selected S/N and resolution values are in most cases dictated by the "limiting cases," i.e., the most difficult star+planet combinations to observe in a specific class of objects. In most tables, the S/N/Res values can be raised for the bright targets, and lowered to curb the integration times for fainter objects. The outcome of our study is summarized in the MIR by showing results averaged over the 7.7–12.7 μm spectral window (equivalent to the classical Johnson photometric *N* band). In addition, in the Appendix we provide results averaged over three spectral bands (5–8.3, 8.3–11, and 11–16 μm); the reader may compare performances of various bands for the listed targets. For hot planets, observations in the NIR (2.5–5 μm band) become feasible (see Section 2.3 with Equation (7)) and planets close to their star can easily be probed in the visible. In such cases, the MIR integration times are followed by NIR and visible results.

3.1. Hot Planets

Gas giants. As a template for the hot Jupiter case, the observed hot gas giant HD 189733b is used. A modeled transmission spectrum analog of primary transit observations and a planet/star contrast ratio, the analog of secondary eclipse measurements, are considered for our simulations (Figure 5). For both cases, integration times are listed in units of number of transits in Table 5, where the modeled hot Jupiter is presented orbiting a sample of stars: a Sun-like G2V star, a warmer F3V star, and HD 189733, a K1/2V-type star (Bouchy et al. 2005). HD 189733 has a magnitude in *V* of 7.67. We extrapolate our results from mag $V = 5$ to $V = 9$, with a resolving power of $R = 300$ and an S/N = 50, chosen for the secondary eclipse, and $R = 100$ and S/N = 50 for the primary transit.

Neptunes. Neptune-like planets are expected to have a similar atmospheric composition as that of gas giants with a smaller radius ($R \sim 0.35\ R_j$). While we do not directly present results for these targets, by comparison with the hot Jupiter scenario, integration times will typically be similar in the primary transit scenario and higher in the secondary eclipse scenario given the relatively smaller radius of the planet.

Super-Earths. We show here two examples: a 2.1 $R_\oplus$ very hot planet in orbit around a G8V star, 55 Cancri e (Winn et al. 2011), and a 1.6 $R_\oplus$, 850 K planet in orbit around a range of M stars with temperature varying between $3055\text{K} \leqslant T \leqslant 3582\text{ K}$. For the latter case, we approximated the planet/star fluxes with blackbody curves to assess feasibility. As mentioned in Section 2.2, primary transit observations for a planet with high gravitational pull might be out of reach (55 Cancri e is reported to be $\sim 8.5\ M_\oplus$), and for this reason we focus on secondary eclipses only. Planet-to-star flux contrasts are plotted in Figure 6 (55 Cancri e in the left panel; 850 K super-Earth in the right panel), accompanied by integration times in Table 6 in the MIR and NIR. For both bands a resolution of $R = 40$ and S/N = 10 were selected.

Observations in the visible. We present here two cases: the case of a hot Jupiter and the case of a hot super-Earth. The reason for our choices is based on Equation (7): reflected light is more prominent for planets close to their star. For the case of the hot super-Earth, we selected a 1.6 $R_\oplus$ planet with a fixed temperature of 850 K and varying albedo values. For the case of the hot Jupiter, we present a fixed orbital distance

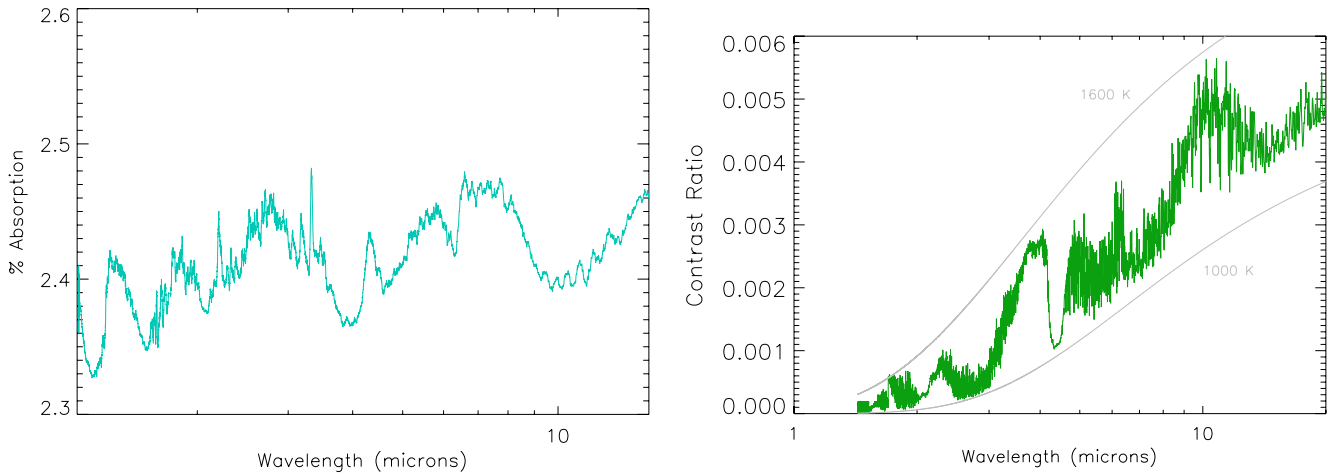

Figure 5. Modeled transmission and emission spectra of HD 189733b (Tinetti et al. 2010b), a hot-Jupiter around a K1/2V star, mag $V = 7.67$. Left: percent absorption of the stellar flux occulted by the planetary atmosphere during the primary transit (transmission spectrum). Right: contrast ratio of the flux from the planet (emission spectrum) over the flux from the star. Blackbody curves at 1000 K and 1600 K are plotted in gray.

(A color version of this figure is available in the online journal.)

Table 5

Integration Times (in Units of "Number of Transits") Needed to Obtain the Specified S/N and Spectral Resolution for a Given Stellar Type/Brightness (in mag V)

Star Type	T (K)	R ($R_\odot$)	Contrast ($\times 10^{-3}$)	Period (days)	$\tau_{\rm transit}$ (hr)	Max. n* (transits)	Integration Time (n. transits) $V=5$	$V=6$	$V=7$	$V=8$	$V=9$
Hot Jupiters—Secondary Eclipse, $R = 300$, S/N = 50, MIR											
F3V†	6740	1.56	1	8.4	2.9	218	7	18	51	156	*lower R*
G2V	5800	1	2.9	3.2	2.36	570	0.7	1.8	4.7	14	45
K1V†	4980	0.8	5.6	2.21	1.8	826	0.2	0.4	1	2.9	9
Hot Jupiters—Primary Transit, $R = 100$, S/N = 50, MIR											
F3V	6740	1.56	0.28	8.4	2.9	218	32	82	213	*lower R*	
G2V	5800	1	0.68	3.2	2.36	570	4	10	26	70	198
K1V	4980	0.8	1	2.21	1.8	826	1.6	4	10	26	72
Hot Jupiter in NIR—Secondary Eclipse, $R = 300$, S/N = 50, NIR											
K1V	4980	0.8	2.6	2.21	1.8	826	0.1	0.2	0.6	1.4	3.5

Notes. The upper portion of the table lists results for the secondary eclipse scenario in the MIR (equivalent to the classical Johnson photometric N band) followed by primary transit results in the MIR, and secondary eclipse results in the NIR (between 2.5 and 5 μm). $\tau_{\rm transit}$ is the transit duration given in hours and "*lower R*" stands for target observable at lower resolution. "†": planet/star systems marked by this sign have additional results listed in the Appendix. "*": the maximum number of transits is computed by dividing a plausible mission lifetime (five years assumed) by the duration of the planet orbital period.

with varying albedo values (corresponding to temperatures ~1200–1500 K). Note that the emission from the planet is negligible at these temperatures when compared with reflection in the visible. Results are given in Tables 7 and 8, with $R = 40$ and S/N = 20 for the hot Jupiter, and $R = 20$ and S/N = 10 for the hot super-Earth.

3.2. Warm Planets

Gas giants. In this section we focus on Neptunes and super-Earths, skipping warm gas giants, which fall between the categories of hot Jupiters and warm Neptunes.

Neptunes. We considered GJ 436b, a 4 $R_\oplus$ planet around an M2.5V-dwarf star, with a radius of 0.46 $R_\odot$ and a magnitude in K of 6.07 (Butler et al. 2004; Gillon et al. 2007) as an example of a warm Neptune. *Spitzer* photometric data have been analyzed and interpreted by Beaulieu et al. (2011), Stevenson et al. (2010), and Knutson et al. (2011); observed results captured by simulated spectra are shown in Figure 7 (primary transit left; secondary eclipse right). Integration times for a primary transit and a secondary eclipse of such a warm Neptune-like planet follow in Table 9.

Super-Earths. GJ 1214b (Charbonneau et al. 2009) is a perfect example of a warm super-Earth orbiting an M star. We show in Figure 8 a simulated transmission spectrum of this planet. Since the available observations for this specific planet are not enough to constrain its true composition and atmospheric characteristics (Bean et al. 2010), our simulations here just show a possible scenario. In Figure 8 we also present planet/star flux contrasts for a 1.6 $R_\oplus$, 500 K planet orbiting a range of M stars (from M1.5V to M5V with temperatures ranging from 3055 K to 3582 K). Both the planet and the stellar contributions here are estimated as blackbodies, and only secondary eclipse results are presented. The integration times are listed in Table 10 in the MIR, with $R = 40$ and S/N = 10.

Table 6
Integration Times (in Units of "Number of Transits") Needed to Obtain the Specified S/N and Spectral Resolution for a Given Stellar Type/Brightness (in mag K When Orbiting M-dwarfs, mag V When Orbiting G Stars)

Hot Super-Earths—Secondary Eclipse, $R = 40$, S/N = 10, MIR											
Star	T	R	Contrast	Period	$\tau_{\rm transit}$	Max. n*	Integration Time (n. transits)				
Type	(K)	($R_\odot$)	($\times 10^{-4}$)	(days)	(hr)	(transits)	$K = 5$	$K = 6$	$K = 7$	$K = 8$	$K = 9$
M0V	3893	0.57	0.7	2.17	1.6	840	38	97	253	689	*lower R.*
M1.5V†	3582	0.42	1.4	1.22	1.1	1494	13	33	87	236	707
M3V	3436	0.30	2.9	0.79	0.8	2300	4.2	11	28	75	225
M4V	3230	0.20	7.2	0.46	0.5	3955	1	2.7	7	19	58
M5V†	3055	0.16	12.2	0.25	0.4	7450	0.5	1.2	3.1	8	25
Hot Super-Earths in NIR—Secondary Eclipse, $R = 40$, S/N = 10, NIR											
M0V	3893	0.57	0.1	2.17	1.6	840	199	499	*lower R.*		
M1.5V	3582	0.42	0.3	1.22	1.1	1494	32	81	203	509	1279
M3V	3436	0.30	0.5	0.79	0.8	2300	15	39	97	243	611
M4V	3230	0.20	1.4	0.46	0.5	3955	3	8	19	18	121
M5V	3055	0.16	2.5	0.25	0.4	7450	1.1	2.8	7	18	45
Hot Super-Earth—Example of 55 Cancri e in the Secondary Transit, $R = 40$, S/N = 10, MIR											
Star	T	R	Contrast	Period	$\tau_{\rm transit}$	Max. n*	Integration Time (n. transits)				
Type	(K)	($R_\odot$)	($\times 10^{-4}$)	(days)	(hr)	(transits)	$V = 5$	$V = 6$	$V = 7$	$V = 8$	$V = 9$
G8V	5243	0.95	1.6	0.74	1.76	2467	1.4	3.4	9	22	58

Notes. The upper portion of the table lists results for the secondary eclipse scenario in the MIR, followed by secondary eclipse results in the NIR. $\tau_{\rm transit}$ is the transit duration given in hours and "*lower R*" stands for target observable at lower resolution. For "†," "∗": see the Notes to Table 5.

Table 7
Integration Times (in Units of "Number of Transits") for a Hot Jupiter Observed in the Visible around a G2V Star

Visible Band Hot Jupiter, with $\zeta = 1$, $R = 40$, S/N = 20										
Albedo	a	Contrast	Period	$\tau_{\rm transit}$	Max. n*	Integration Time (n. of transits)				
Value	(a.u.)	($\times 10^{-4}$)	(days)	(hr)	(transits)	$V = 5$	$V = 6$	$V = 7$	$V = 8$	$V = 9$
0.1		0.31				7	18	44	110	278
0.3		0.92				0.8	1.9	4.9	12	31
0.5	0.031	1.54	4.7	2.36	570	0.3	0.7	1.8	4.5	11
0.7		2.16				0.1	0.4	0.9	2.3	6

Notes. The orbital distance is fixed and the planetary temperature varies with the albedo. For the studies presented here, we have considered full illumination ($\zeta = 1$), and values of $R = 40$ and S/N = 20. When the planet is not fully illuminated ($\zeta < 1$), longer integration times are needed for the same parameters. "∗": see the Notes to Table 5.

Table 8
Integration Times (in Units of "Number of Transits") for a Hot Super-Earth (850 K) Observed in the Visible around an M4.5V Star

Visible Band Hot Super-Earth, with $\zeta = 1$, $R = 20$, S/N = 10										
Albedo	a	Contrast	Period	$\tau_{\rm transit}$	Max. n*	Integration Time (n. of transits)				
Value	(a.u.)	($\times 10^{-4}$)	(days)	(hr)	(transits)	$K = 5$	$K = 6$	$K = 7$	$K = 8$	$K = 9$
0.1	0.006	0.15	0.47	0.8	3916	426	1161	2917	*lower R.*	
0.3	0.006	0.58	0.39	0.7	4728	35	89	223	560	1407
0.5	0.005	1.35	0.30	0.7	6085	7	16	41	103	260
0.7	0.004	3.16	0.20	0.6	8927	1.4	3.5	9	22	55

Notes. Here the planetary temperature is fixed and the orbital distance varies with the albedo. For the studies presented here, we have considered full illumination ($\zeta = 1$), and values of $R = 20$ and S/N = 10. When the planet is not fully illuminated ($\zeta < 1$), longer integration times are needed for the same parameters. "*lower R*" stands for target observable at lower resolution. "∗": see the Notes to Table 5.

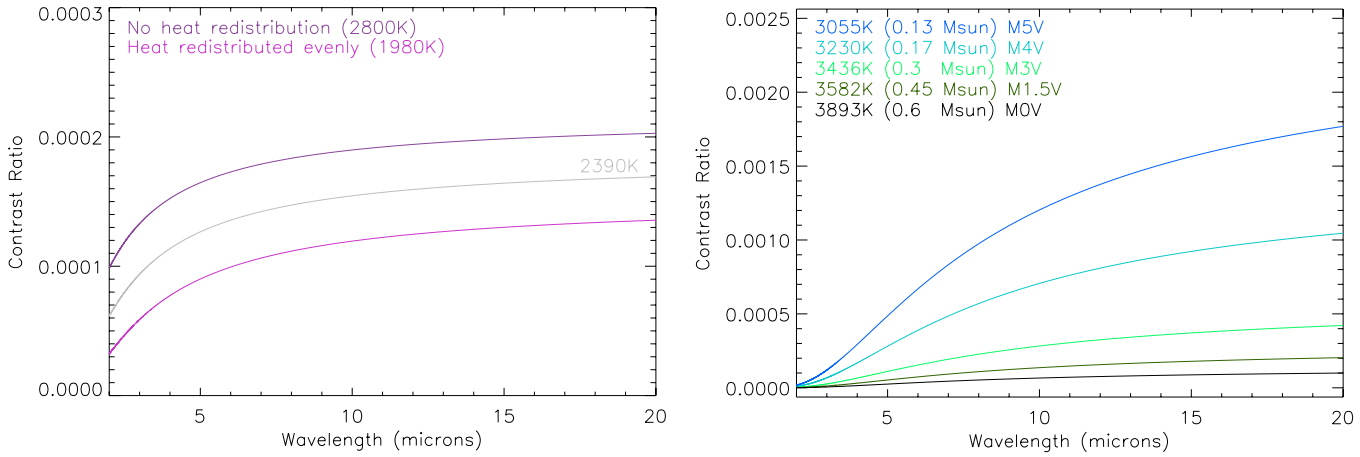

Figure 6. Left: secondary eclipse simulated signal for 55 Cancri e, a 2.1 $R_\oplus$ hot super-Earth orbiting a G8V star. The atmospheric temperature could vary between 2800 K and 1980 K, depending on the heat redistribution (Winn et al. 2011). Both possibilities are presented, alongside an intermediate case of a 2390 K atmosphere used for our results. Right: secondary eclipse signal for a hot super-Earth (850 K, 1.6 $R_\oplus$) orbiting a selection of M stars (from M1.5V to M5V). For the two figures, both the planet and the stellar contributions here are estimated as blackbodies. While this description is too simplistic to capture the properties of a real, specific case, for feasibility tests we do not want to rely on too narrow assumptions.

(A color version of this figure is available in the online journal.)

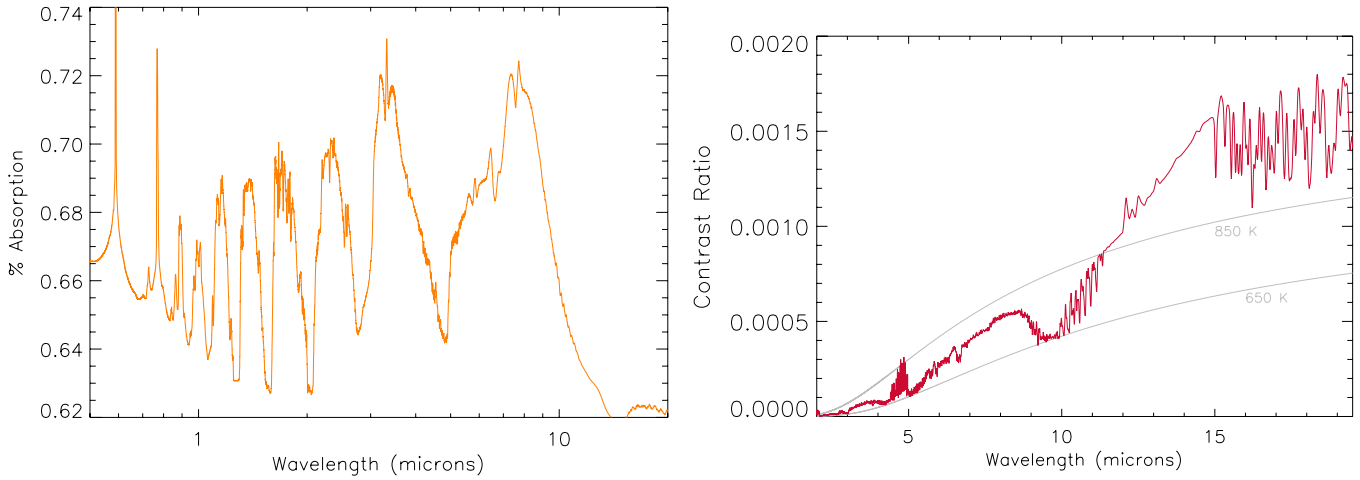

Figure 7. Modeled GJ 436b (Beaulieu et al. 2011; Stevenson et al. 2010), a warm Neptune around a M2.5V star, mag $K = 6.07$. Left: percent absorption of the stellar flux occulted by the planetary atmosphere during the primary transit. Right: contrast ratio of the flux from the planet over the flux from the star. Blackbody curves at 650 K and 850 K are plotted in gray.

(A color version of this figure is available in the online journal.)

Table 9
Integration Times (in Units of "Number of Transits") Needed to Obtain the Specified S/N and Spectral Resolution for a Given Stellar Type/Brightness (in mag K)

Star Type	T (K)	R ($R_\odot$)	Contrast ($\times 10^{-4}$)	Period (days)	τ_{trans} (hr)	Max. n* (transits)	R/S/N	Integration Time (n. transits) $K=5$	$K=6$	$K=7$	$K=8$	$K=9$
Warm Neptune—Secondary Eclipse, $R = 50$–100, S/N = 30–50, MIR												
M2.5V†	3684	0.46	4.6	2.64	1.03	691	100/50	80	207	563	*lower Res.*	
							50/30	14	36	95	263	*low R*
Warm Neptune—Primary Transit, $R = 50$–100, S/N = 30–50, MIR												
M2.5V	3684	0.46	10	2.64	1.03	691	100/50	17	44	120	358	*low R*
							50/30	3	8	20	56	173

Notes. The upper part of the table lists results for the secondary eclipse scenario in the MIR, followed by primary transit results in the MIR. Both parts show two selections of S/N and resolution values. $\tau_{transit}$ is the transit duration given in hours, and "*lower R*" stands for target observable at lower resolution. For "†," "∗": see the Notes to Table 5.

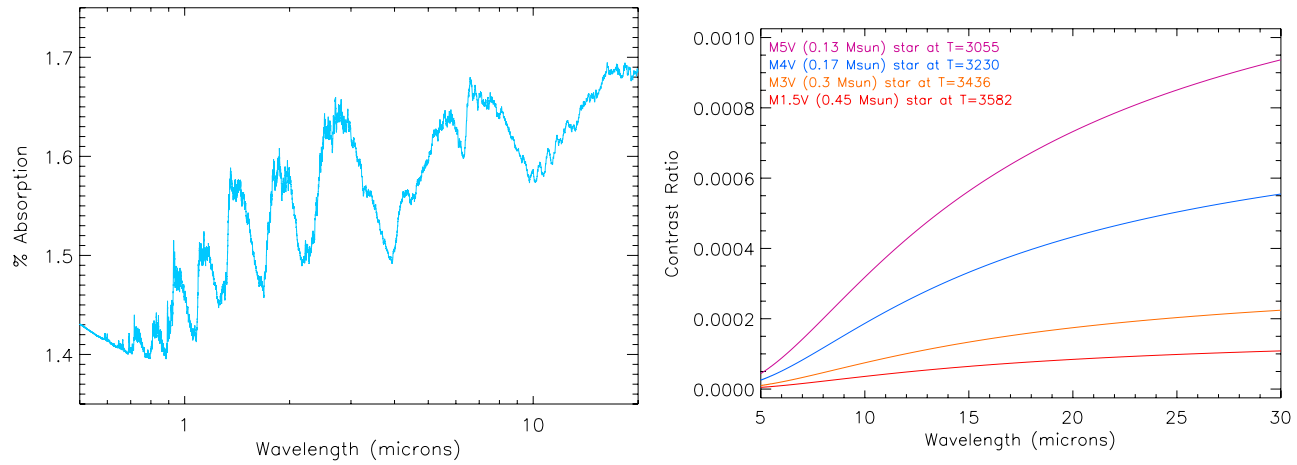

Figure 8. Left: simulated transmission spectrum for the warm super-Earth GJ 1214b, in units of percent absorption of the stellar flux. Right: secondary eclipse signal from a warm super-Earth (500 K, 1.6 $R_\oplus$) orbiting a range of M stars, from M1.5V to M5V with temperatures ranging from 3055 K to 3582 K.

(A color version of this figure is available in the online journal.)

Table 10

Integration Times (in Units of "Number of Transits") Needed to Obtain the Specified S/N and Spectral Resolution for a Given Stellar Type/Brightness (in mag *K*)

Warm Super-Earths—Secondary Eclipse, $R = 40$, S/N = 10, MIR											
Star	T	R	Contrast	Period	$\tau_{transit}$	Max. n*	Integration Time (n. transits)				
Type	(K)	($R_\odot$)	($\times 10^{-4}$)	(days)	(hr)	(transits)	$K = 5$	$K = 6$	$K = 7$	$K = 8$	$K = 9$
M1.5V	3582	0.42	0.4	6	1.9	304	52	131	335	*low R*	*ph*
M3V	3436	0.30	0.8	3.9	1.3	468	18	44	114	298	*low R*
M4V†	3230	0.20	1.9	2.27	0.9	804	4	10	26	69	192
M5V†	3055	0.16	3.3	1.57	0.7	1163	1.8	4.6	12	31	85
Warm Super-Earth—Example of GJ1214b in the Primary Transit, $R = 40$, S/N = 10, MIR											
M4.5V	2949	0.21	27	1.58	0.88	1155	0.1	0.1	0.3	0.8	2.3

Notes. The upper part of table lists results for the secondary eclipse scenario in the MIR, followed by secondary eclipse results in the NIR. $\tau_{transit}$ is the transit duration given in hours, "*lower R*" stands for target observable at lower resolution, and *ph* stands for photometry. "†," "∗": see the Notes to Table 5.

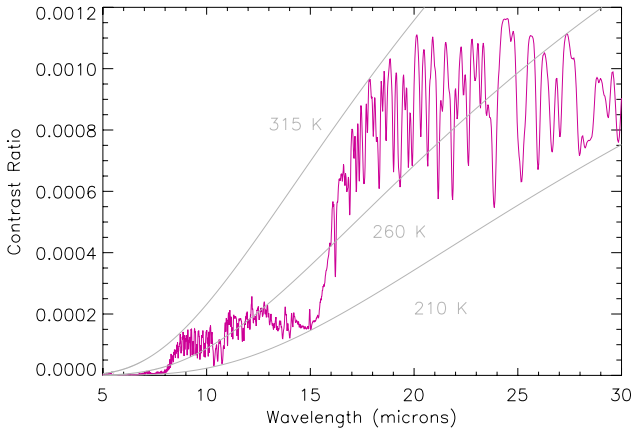

Figure 9. Secondary eclipse signal from a conceivable habitable-zone Jupiter around a K4V, 4780 K star—such as HAT-P-11. Blackbody curves at 210 K, 260 K, and 315 K are plotted in gray.

(A color version of this figure is available in the online journal.)

3.3. Habitable Zone Planets

Gas giants. We present here the case of a hypothetical "cool" Jupiter, in the HZ of a K4V star. Figure 9 shows our simulated secondary eclipse spectrum, with an atmosphere in which we have included water vapor, methane, hydrocarbons, CO and CO_2, and a thermal profile with temperature decreasing with altitude. In Figure 9, the departure from the (315 K) blackbody is noticeable. While our assumptions here are reasonable, this is just one possible scenario, and completeness is beyond the scope of this paper. Integration times are listed in Table 11 for different stellar brightnesses.

Neptunes. We skip the case of an HZ Neptune, as the secondary eclipse falls between the categories of an HZ Jupiter and an HZ super-Earth. In the case of primary transits, by contrast, we expect a much more favorable result, as indicated in Table 3.

Super-Earths. Here we present a 1.8 $R_\oplus$ telluric planet, with three plausible atmospheres, as explained in Section 2.1: Earth-like, Venus-like, and hydrogen-rich (i.e., small Neptune). Figure 10 shows the planet-to-star flux contrast obtained for a 1.8 $R_\oplus$ super-Earth orbiting an M4.5V star with $T = 3150$ K, with the three mentioned atmospheres in two spectral resolutions: $R = 200$ and $R = 20$. Blackbody curves at 200, 250, 300, and 350 K are included. The change in contrast for the different atmospheric cases is noticeable; for instance, the presence of water vapor in the Earth-like and small Neptune cases marks a sharper departure from the blackbody curve. H_2O, CO_2, and ozone absorption are still detectable even at very low resolution, but less abundant hydrocarbon species become more difficult to capture. Table 12 lists integration times in the MIR for the case of a 300 K atmosphere and a range of stars spanning type and brightness. While the resolution of $R = 10$ and S/N = 5 was selected to cover the broadest range of stellar types in the table,

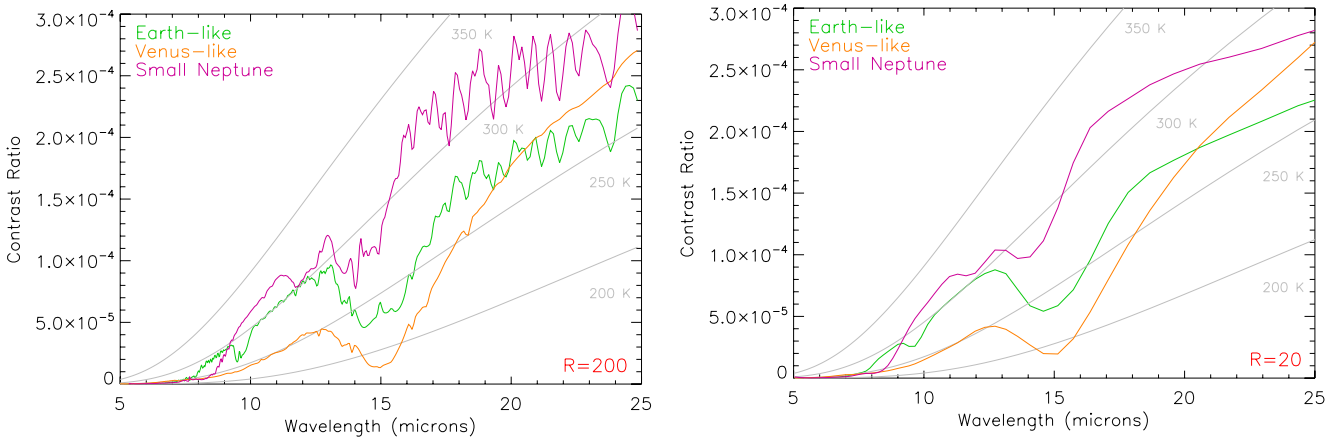

Figure 10. Left: Earth-like, Venus-like, and small Neptune secondary eclipse spectra at $R = 200$, with marked blackbody contrast curves as temperature indicators (from left to right: 350, 300, 250, and 200 K). The three atmospheres belong to a 1.8 $R_\oplus$ super-Earth around an M4.5V star (at $T = 3150$ K). Right: the same case at a resolution of $R = 20$.

(A color version of this figure is available in the online journal.)

Table 11
Integration Times (in Units of "Number of Transits") Needed to Obtain the Specified S/N and Spectral Resolution for a Given Brightness (in mag *V*)

Cool Jupiter—Secondary Eclipse, $R = 20$–40, S/N = 10, MIR												
Star	T	R	Contrast	Period	$\tau_{\rm trans.}$	Max. n*	R/S/N	Integration Time (n. of transits)				
Type	(K)	($R_\odot$)	($\times 10^{-4}$)	(days)	(hr)	(transits)		$V = 5$	$V = 6$	$V = 7$	$V = 8$	$V = 9$
K4V†	4780	0.75	1.5	101.6	6.9	18	40/10	0.3	0.6	1.6	4.1	11
							20/10	0.1	0.3	0.8	2	5

Notes. The results are given in the MIR with two selections of S/N and resolution. $\tau_{\rm trans.}$ is the transit duration given in hours. Note that the orbital period for a planet in the HZ of a K4V star is more than 100 days, so the observation can be repeated less than 20 times in five years. "†," "∗": see the Notes to Table 5.

Table 12
Integration Times (in Units of "Number of Transits") Needed to Obtain the Specified S/N and Spectral Resolution for a Given Stellar Type/Brightness (in mag *K*) in the MIR

HZ Super-Earth—Secondary Eclipse, $R = 10$, S/N = 5, MIR											
Star	T	R	Contrast	Period	$\tau_{\rm transit}$	Max. n*	Integration Time (n. transits)				
Type	(K)	($R_\odot$)	($\times 10^{-5}$)	(days)	(hr)	(transits)	$K = 5$	$K = 6$	$K = 7$	$K = 8$	$K = 9$
M2.5V	3475	0.34	1.1	23.7	2.6	77	54			*photometry*	
M3V	3436	0.30	1.4	20.6	2.3	88	37			*photometry*	
	3380	0.26	1.9	17.3	2.1	105	22	55		*photometry*	
M4V†	3230	0.20	3.5	12	1.6	152	9	22	54	140	*ph*
	3150	0.17	4.6	10	1.4	182	6	14	36	94	*ph*
M5V†	3055	0.16	6	8.3	1.3	220	3.6	9	23	60	158
	2920	0.14	8.5	6.4	1.1	286	2.2	5	14	36	94

Notes. $\tau_{\rm transit}$ is the transit duration given in hours and *ph* stands for photometry, where a few wavelengths can be probed for the most challenging targets. For "†","∗": see the Notes to Table 5.

the cooler stars in the table will allow for higher S/N/resolution values.

4. DISCUSSION

4.1. Stellar Variability

Our simulations do not include the effects of stellar variability on transit observations. *Kepler* is reaching 200 ppm minute^{-1} on a $V = 11$ mag star and 40 ppm minute^{-1} on a $V = 7$ mag star. The most up-to-date information about variability comes from the studies of Basri et al. (2010, 2011) based on the analysis of 100,000 stars (first release of 43 days of *Kepler* data). For timescales between 3 and 16 days, the authors showed that 57% of the G stars are active and tend to be more active than the Sun (up to twice the activity level is typical). This fraction increases to 87% of the K- and M-dwarfs (Figure 4 of Basri et al. 2010). The peak of the histogram of amplitude distribution is centered at 2 mmag. Scatter plots from Basri et al. show that for K and M stars the dominant source of scatter is variability, not Poisson noise. The bulk of the periodicities are found at periods larger than 10 days, with amplitudes ranging from 1–10 mmag. Ciardi et al. (2011) found that 80% of the M-dwarfs have dispersion less than 500 ppm over a period of 12 hr, while G-dwarfs are the most stable group down to 40 ppm.

It is important to note here that photometric variability is significantly lower in the near-infrared than in the *Kepler* band (Agol et al. 2010; Knutson et al. 2011) because of the lower contrast between spots and the stellar photosphere at larger wavelengths. For instance, Agol et al. (2010) measured that

the infrared flux variations in the case of the active K star HD 189733 are about 20% of the optical variations. This is in agreement with the theoretical estimates by Ballerini et al. (2011).

Most importantly, all the timescales related to stellar activity patterns are very different from the timescales associated with single transit observations (a few hours), and thus can easily be removed. CoRoT-7 b provides a good example. The activity modulations are of the order of 2% and yet *CoRoT* managed to find a transit with a depth of 0.03%. This was made possible by the continuous monitoring provided by *CoRoT* and the different timescale compared with the transit signal that allowed for the removal of the activity effects and the discovery of variations smaller than the overall modulation by a factor of 70. The same situation has been encountered in the list of 1200 *Kepler* candidates announced recently, in which stellar activity modulations and transit events have been disentangled, often with the former being far greater than the latter.

In conclusion, the overall (random) photometric jitter of the star should not be a crucial factor with the right strategy to adequately correct for modulations caused by spot variations. Time series can be used as an "activity monitor" by the visible part of the spectrum. As mentioned in Section 2.4, systematic differences in the stellar flux could hamper multiple transit combinations. However, where primary transit observations are subject to these effects, secondary eclipse observations are preferred as they are immune to them.

4.2. Planetary Variability

Upper limits on eclipse variability have been reported by Agol et al. (2010) and Knutson et al. (2011). We do not know the nature of this variability, but the chance of observing multiple spectra rather than photometric bands might be helpful in exploring the potential sources of atmospheric variability (thermal changes? chemical changes? clouds/hazes?) for the most favorable targets. In the case of faint targets, for which co-adding eclipse observations is necessary, only spatially/temporally averaged information will be available. From the experience with the planets in our own solar system, this information, although more limited, is expected to still be very significant.

4.3. Stellar Population

The integration times required to study HZ super-Earths (given in Table 12) show that characterization of these targets is possible provided they orbit late-type dwarfs. While bright targets are preferred, as they provide a higher photon signal, our results cover a range of magnitudes from $K = 5$ to $K = 9$. In parallel, the M-type population found in the RECONS catalog (RECONS 2011), which lists 100 stars up to 6.6 pc in the Sun's local neighborhood, is mostly formed of bright targets with a significant fraction having magnitudes between $K = 4$ and $K = 6$ (see Figure 3). However, extrapolation from the catalog up to magnitude $K = 9$ yields a much larger stellar population that can be studied for super-Earths. Thus, combining the feasibility of studying targets up to $K = 9$, while keeping a preference for brighter sources, and the greater amount of fainter stars up to mag $K = 9$ creates a common area ideal for super-Earth observations centered around the $K = 7$–8 magnitude region. A mission that aims to characterize HZ super-Earths should have detectors optimized for this magnitude range.

4.4. Instrument Transmission

Throughout this paper we have considered an instrumental transmission value of 0.7. In practical applications, many factors can reduce this transmission value. While most of the cases presented allow for slightly longer observations, the most challenging category of HZ super-Earths will require high instrumental transmission values to remain feasible. Instrument designs with high levels of transmission, such as Fourier transform spectrographs, can be considered a possibility for the characterization of these most challenging targets.

4.5. Systematic Effects

We presented here idealized cases where systematic errors (such as detector time constants, pointing jitter, re-acquisition errors, temperature fluctuations, etc.) were not accounted for. Instrumental settings for our results from the visible to the infrared were based on available technology and can be considered realistic. With these considerations, the results presented in this paper highlight that in the coming years HZ super-Earths are realistically within reach. In future work, we will update our models as information on the systematic effects of specific instruments becomes available.

5. CONCLUSIONS

In this paper we have presented a detailed study of the performances and tradeoffs of an M-class transit spectroscopy mission dedicated to the observation of exoplanetary atmospheres. We have demonstrated that, in principle, with a 1.2/1.4 m space telescope performing simultaneous spectroscopy from the visible to the mid-IR, we are able to secure the characterization of a plethora of exoplanets, ranging from hot, gaseous ones down to temperate ones approaching the size of Earth. According to our simulations, the spectra of hot Jupiters orbiting F-, G-, and K-type stars with V mag brighter than 10 can be obtained by integrating from a fraction of transit up to a few tens of transits to reach a spectral resolution of 300 and S/N = 50. HZ super-Earths are undoubtedly the most challenging category of targets due to their small size, low temperature, and relatively large separation from the star. We show, however, that these targets can be observed at low resolution in the mid-IR, provided their hosting star is a bright M-dwarf. While most of the Sun's neighborhood is composed of these late-type stars, efforts still need to be directed at increasing the number of low-mass stars known and constraining their properties. The 2MASS catalog sample, completed with current and planned dedicated ground-based surveys, as well as space missions such as *WISE* and *Gaia* should offer a viable solution to this critical issue in the next five years. In future work, we will update our current instrument models by including a more realistic treatment of the systematics.

We thank Laura Affer for her work on analyzing 2MASS data through color–color diagrams, Ingo Waldmann for discussions on signal-to-noise issues, and in particular the anonymous referee for helpful comments.

APPENDIX

In addition to the numbers presented throughout the paper for a 1.4 m telescope, we provide here two supplementary sets of results for a 1.2 m telescope. We detail in Table 13 the parameters adopted for the two cases. The results are displayed in the following way: Number of transits: Case 1 *(Case 2)*.

Table 13
List of Parameters Used in the Two Sets of Appendix Results

	Case 1		Case 2
Detector Used	SOFRADIR		RAYTHEON
	LWIR	VLWIR	JWST Si:As
Spectral range considered (μm)	5–11	11–16	5–16
Full well capacity (electrons)	2×10^7	5×10^6	2×10^5
Dark current (electrons s^{-1} $pixel^{-1}$)	500	300	0.2
Quantum efficiency (electrons $photon^{-1}$)	0.7	0.7	0.7
Readout noise (electrons $pixel^{-1}$ $readout^{-1}$)	1000	1000	15
Readout time (s)	0.03	0.01	3
Telescope temperature (K)	<60	<60	<60
Instrument temperature (K)	45	45	45
Telescope transmission	0.9	0.9	0.85
Instrument transmission	0.7	0.7	0.4

Notes. In the first case, two detectors are needed to cover the 5–16 μm range, while for the second set of results, which represents an alternate design of the instruments, one detector is used for the full range. The results are split into four columns representing wavelength bands used. The first column lists values in the photometric *N* band, which is also the band used for results presented throughout the paper, followed by three channels: 5–8.3 μm, 8.3–11 μm, and 11–16 μm. A 30 μm pixel size and 2 illuminated pixels per spectral element are assumed. (For the *N* band, 7.7–12.7 μm, we have used the LWIR setting values.) In the case of the VLWIR detector, we have used a dark current value of 300 electrons s^{-1} $pixel^{-1}$ considering existing technologies and expected future capabilities. Further discussion on these values can be found in Section 4.4.

A.1. 1.2 m Telescope, Hot Planets

See Table 14 for results.

Table 14
Hot Planets

Bands:	*N* (7.7 to 12.7)	5 to 8.3	8.3 to 11	11 to 16
(1) Contrasts:	1.01E−03	5.13E−04	8.34E−04	7.21E−04
$V = 5$	9.56 *(15.71)*	12.62 *(21.22)*	13.60 *(22.38)*	41.05 *(58.11)*
$V = 6$	25.29 *(39.49)*	32.30 *(53.31)*	35.94 *(56.21)*	111.60 *(157.43)*
$V = 7$	71.63 *(99.33)*	84.94 *(133.92)*	101.47 *(141.22)*	LR *(LR)*
$V = 8$	LR *(LR)*	LR *(LR)*	LR *(LR)*	LR *(LR)*
$V = 9$	LR *(LR)*	LR *(LR)*	LR *(LR)*	LR *(LR)*
(2) Contrasts:	5.56E−03	2.89E−03	4.61E−03	3.93E−03
$V = 5$	0.21 *(0.36)*	0.27 *(0.50)*	0.30 *(0.50)*	0.90 *(1.28)*
$V = 6$	0.54 *(0.89)*	0.67 *(1.13)*	0.77 *(1.26)*	2.35 *(3.33)*
$V = 7$	1.44 *(2.24)*	1.73 *(2.84)*	2.04 *(3.18)*	6.42 *(9.05)*
$V = 8$	4.12 *(5.64)*	4.55 *(7.14)*	5.80 *(7.98)*	19.33 *(27.07)*
$V = 9$	13.42 *(14.23)*	12.76 *(17.95)*	18.81 *(20.06)*	68.83 *(95.35)*
(3) Contrasts:	1.38E−04	8.61E−05	1.32E−04	1.69E−04
$K = 5$	17.86 *(30.06)*	15.30 *(36.55)*	19.15 *(32.23)*	25.47 *(36.29)*
$K = 6$	45.71 *(75.54)*	38.68 *(65.21)*	48.97 *(80.96)*	66.87 *(95.81)*
$K = 7$	120.18 *(189.99)*	98.68 *(163.79)*	128.52 *(203.40)*	186.32 *(270.04)*
$K = 8$	335.66 *(478.83)*	257.50 *(411.44)*	357.59 *(511.12)*	583.75 *(863.62)*
$K = 9$	1056.31 *(1212.80)*	707.50 *(1033.57)*	1117.56 *(1285.18)*	LR *(LR)*
(4) Contrasts:	1.22E−03	7.78E−04	1.17E−03	1.48E−03
$K = 5$	0.63 *(1.06)*	0.51 *(1.23)*	0.67 *(1.13)*	0.90 *(1.29)*
$K = 6$	1.61 *(2.66)*	1.28 *(2.16)*	1.72 *(2.84)*	2.73 *(3.40)*
$K = 7$	4.23 *(6.69)*	3.27 *(5.44)*	4.51 *(7.13)*	6.60 *(9.56)*
$K = 8$	11.82 *(16.87)*	8.54 *(13.65)*	12.54 *(17.92)*	20.63 *(30.52)*
$K = 9$	37.19 *(42.72)*	23.42 *(34.30)*	39.18 *(45.07)*	77.42 *(117.64)*

Notes. (1) Integration times in number of transits for a hot Jupiter orbiting a F3.0V star. The four columns compare integration times in different bands for the same target. The contrast value and number of resolution elements are given for each band. The five rows list results for the specified star with varying magnitude (here in mag. *V*). The star temperature used is 6740 K, and the transit duration assumed is 2.90 hr. A spectral resolution of 300 and an S/N value of 50 are used. A dash "-" signifies that the number of transits required is over the maximum number of transits that can be covered over a mission lifetime. "LR" stands for lower resolution, and is indicated when observations need to be done at a lower spectral resolution to fit within the time constrains of a mission, and "phot" stands for photometry at selected wavelengths, where lower resolution is not feasible. (2) Planet: hot jupiter; star: K1V; temp: 4900 K; $R = 300$; S/N = 50. (3) Planet: hot SE; star: M1.5V; temp: 3582 K; $R = 40$; S/N = 10. (4) Planet: hot SE; star: M5V; temp: 3055 K; $R = 40$; S/N = 10.

A.2. 1.2 m Telescope, Warm Planets

See Table 15 for results.

Table 15
Warm Planets

Bands:	*N* (7.7 to 12.7)	5 to 8.3	8.3 to 11	11 to 16
(1) Contrasts:	4.61E−04	3.10E−04	4.10E−04	1.28E−03
$K = 5$	19.39 *(32.52)*	14.12 *(27.06)*	23.82 *(39.97)*	5.31 *(7.57)*
$K = 6$	49.84 *(81.74)*	35.75 *(60.11)*	61.18 *(100.40)*	14.03 *(20.07)*
$K = 7$	132.40 *(205.61)*	91.55 *(151.00)*	162.21 *(252.24)*	39.56 *(57.18)*
$K = 8$	378.10 *(518.31)*	241.00 *(379.32)*	461.30 *(633.88)*	126.66 *(186.27)*
$K = 9$	LR *(LR)*	675.07 *(LR)*	LR *(LR)*	490.38 *(LR)*
(2) Contrasts:	1.93E−04	7.12E−05	1.75E−04	2.94E−04
$K = 5$	5.55 *(9.40)*	13.49 *(65.35)*	6.62 *(11.22)*	5.06 *(7.22)*
$K = 6$	14.08 *(23.63)*	34.00 *(65.35)*	16.79 *(28.18)*	13.13 *(18.86)*
$K = 7$	36.22 *(59.41)*	86.06 *(144.73)*	43.14 *(70.78)*	35.62 *(51.91)*
$K = 8$	96.34 *(149.68)*	220.38 *(363.54)*	114.42 *(177.86)*	106.09 *(159.04)*
$K = 9$	275.81 *(378.73)*	580.07 *(LR)*	325.63 *(447.17)*	371.25 *(580.26)*
(3) Contrasts:	3.29E−04	1.22E−04	2.98E−04	4.98E−04
$K = 5$	2.46 *(4.17)*	5.86 *(28.50)*	2.93 *(4.96)*	2.25 *(3.21)*
$K = 6$	6.24 *(10.47)*	14.76 *(28.51)*	7.43 *(12.47)*	5.84 *(8.39)*
$K = 7$	16.05 *(26.33)*	37.36 *(62.82)*	19.09 *(31.32)*	15.84 *(23.08)*
$K = 8$	42.69 *(66.33)*	95.65 *(157.81)*	50.62 *(78.69)*	47.15 *(70.67)*
$K = 9$	122.22 *(167.84)*	251.71 *(396.40)*	144.07 *(197.85)*	164.88 *(257.66)*

Notes. See Table 14 for additional explanation. (1) Planet: warm Neptune; star: M2.5V; temp: 3480 K; $R = 50$; S/N = 30. (2) Planet: warm SE; star: M4V; temp: 3230 K; $R = 20$; S/N = 10. (3) Planet: warm SE; Star: M5V; temp: 3055 K; $R = 20$; S/N = 10.

A.3. 1.2 m Telescope, HZ Planets

See Table 16 for results.

Table 16
HZ Planets

Bands:	*N* (7.7 to 12.7)	5 to 8.3	8.3 to 11	11 to 16
(1) Contrasts:	1.53E−04	2.12E−06	1.27E−04	1.58E−04
$V = 5$	0.35 *(1.86)*	phot *(-)*	0.49 *(2.70)*	0.69 *(1.75)*
$V = 6$	0.87 *(1.86)*	- *(-)*	1.24 *(2.70)*	1.74 *(2.47)*
$V = 7$	2.21 *(3.72)*	- *(-)*	3.12 *(5.26)*	4.44 *(6.32)*
$V = 8$	5.65 *(9.36)*	- *(-)*	7.98 *(13.22)*	11.63 *(16.66)*
$V = 9$	14.83 *(LR)*	- *(-)*	LR *(LR)*	LR *(LR)*
(2) Contrasts:	3.54E−05	4.97E−06	2.89E−05	8.15E−05
$K = 5$	11.60 *(36.69)*	phot *(-)*	16.91 *(59.39)*	4.60 *(7.84)*
$K = 6$	29.28 *(52.81)*	phot *(-)*	42.68 *(76.96)*	11.87 *(18.20)*
$K = 7$	74.47 *(132.80)*	- *(-)*	108.43 *(phot)*	31.75 *(49.50)*
$K = 8$	phot *(-)*	- *(-)*	phot *(-)*	92.00 *(phot)*
(3) Contrasts:	8.46E−05	1.21E−05	6.92E−05	1.93E−04
$K = 5$	2.95 *(10.42)*	47.51 *(-)*	4.29 *(15.55)*	1.18 *(2.08)*
$K = 6$	7.46 *(13.87)*	119.51 *(-)*	10.83 *(20.15)*	3.04 *(4.81)*
$K = 7$	18.96 *(34.87)*	phot *(-)*	27.53 *(50.61)*	8.13 *(13.07)*
$K = 8$	49.10 *(87.83)*	phot *(-)*	71.12 *(127.18)*	23.53 *(39.10)*
$K = 9$	132.62 *(222.11)*	- *(-)*	191.12 *(phot)*	78.75 *(137.79)*

Notes. See Table 14 for additional explanation. (1) Planet: HZ Jup; star: K4V; temp: 4780 K; $R = 40$; S/N = 10. (2) Planet: HZ SE; star: M4V, temp: 3230 K; $R = 10$; S/N = 5. (3) Planet: HZ SE; star: M5.5V; temp: 2920 K; $R = 10$; S/N = 5.

REFERENCES

Agol, E., Cowan, N. B., Knutson, H. A., et al. 2010, ApJ, 721, 1861
Ballerini, P., Micela, G., Lanza, A., & Pagano, I. 2011, A&A, submitted
Baraffe, I., Chabrier, G., Allard, F., & Hauschildt, P. H. 1998, A&A, 337, 403
Barber, R. J., Tennyson, J., Harris, G. J., & Tolchenov, R. N. 2006, MNRAS, 368, 1087
Basri, G., Walkowicz, L. M., Batalha, N., et al. 2010, ApJ, 713, L155
Basri, G., Walkowicz, L. M., Batalha, N., et al. 2011, AJ, in press, arXiv:1008.1092v2
Bean, J. L., Miller-Ricci Kempton, E., & Homeier, D. 2010, Nature, 468, 669
Beaulieu, J. P., Carey, S., Ribas, I., & Tinetti, G. 2008, ApJ, 677, 1343
Beaulieu, J. P., Kipping, D. M., Batista, V., et al. 2010, MNRAS, 409, 963
Beaulieu, J.-P., Tinetti, G., Kipping, D. M., et al. 2011, ApJ, 731, 16
Borucki, W. J., Koch, D., Jenkins, J., et al. 2009, Science, 325, 709
Borucki, W. J., Koch, D. G., Basri, G., et al. 2011, submitted, arXiv: 1102.0541v2

Bouchy, F., Udry, S., Mayor, M., et al. 2005, A&A, 444, L15
Brown, T. M., Charbonneau, D., Gilliland, R. L., Noyes, R. W., & Burrows, A. 2001, ApJ, 552, 699
Butler, R. P., Vogt, S. S., Marcy, G. W., et al. 2004, ApJ, 617, 580
Casertano, S., Lattanzi, M. G., Sozzetti, A., et al. 2008, A&A, 482, 699
Charbonneau, D., Berta, Z. K., Irwin, J., et al. 2009, Nature, 462, 891
Charbonneau, D., Brown, T. M., Noyes, R. W., & Gilliland, R. L. 2002, ApJ, 568, 377
Ciardi, D. R., von Braun, K., Bryden, G., et al. 2011, AJ, 141, 108
Cowan, N. B., & Agol, E. 2008, ApJ, 678, L129
Cowan, N. B., & Agol, E. 2011, ApJ, 726, 82
Cowan, N. B., Agol, E., & Charbonneau, D. 2007, MNRAS, 379, 641
Crossfield, I. J. M., Hansen, B. M. S., Harrington, J., et al. 2010, ApJ, 723, 1436
Delfosse, X., Forveille, T., Ségransan, D., et al. 2000, A&A, 364, 217
Gaidos, E., & Williams, D. M. 2004, New Astron., 10, 67
Gillon, M., Pont, F., Demory, B.-O., et al. 2007, A&A, 472, L13
Grasset, O., Schneider, J., & Sotin, C. 2009, ApJ, 693, 722
Grillmair, C. J., Burrows, A., Charbonneau, D., et al. 2008, Nature, 456, 767
Harrington, J., Hansen, B. M., Luszcz, S. H., et al. 2006, Science, 314, 623
Iro, N., & Deming, L. D. 2010, ApJ, 712, 218
Knutson, H. A., Charbonneau, D., Allen, L. E., et al. 2007a, Nature, 447, 183
Knutson, H. A., Charbonneau, D., Cowan, N. B., et al. 2009a, ApJ, 703, 769
Knutson, H. A., Charbonneau, D., Cowan, N. B., et al. 2009b, ApJ, 690, 822
Knutson, H. A., Charbonneau, D., Noyes, R. W., Brown, T. M., & Gilliland, R. L. 2007b, ApJ, 655, 564
Knutson, H. A., Madhusudhan, N., Cowan, N. B., et al. 2011, ApJ, 735, 27
Kurucz, H. L. 1995, in ASP Conf. Ser. 81, Laboratory and Astronomical High Resolution Spectra, ed. A. J. Sauval, R. Blomme, & N. Grevesse (San Francisco, CA: ASP), 17
Langton, J., & Laughlin, G. 2008, ApJ, 674, 1106
Lépine, S., & Gaidos, E. 2011, AJ, 142, 138
Lewis, N. K., Showman, A. P., Fortney, J. J., et al. 2010, ApJ, 720, 344
Perryman, M. A. C., & ESA (ed.) 1997, The HIPPARCOS and TYCHO Catalogues. Astrometric and Photometric Star Catalogues Derived from the ESA HIPPARCOS Space Astrometry Mission (ESA Special Publication, Vol. 1200; Noordwijk: ESA)
Rauscher, E., Menou, K., Seager, S., et al. 2007, ApJ, 664, 1199
RECONS 2011, The Research Consortium on Nearby Stars, http://www.recons.org
Redfield, S., Endl, M., Cochran, W. D., & Koesterke, L. 2008, ApJ, 673, L87
Rothman, L. S., Gordon, I. E., Barber, R. J., et al. 2010, J. Quant. Spectrosc. Radiat. Transfer, 111, 2139
Schneider, J. 2011, The Extrasolar Planets Encyclopaedia, http://exoplanet.eu/catalog.php
Seager, S., & Mallen-Ornelas, G. 2003, ApJ, 585, 1038
Seager, S., & Sasselov, D. D. 2000, ApJ, 537, 916
Selsis, F., Wordsworth, R. D., & Forget, F. 2011, A&A, 532, A1
Snellen, I. A. G., Albrecht, S., de Mooij, E. J. W., & Le Poole, R. S. 2008, A&A, 487, 357
Snellen, I. A. G., de Kok, R. J., de Mooij, E. J. W., & Albrecht, S. 2010, Nature, 465, 1049
Snellen, I. A. G., de Mooij, E. J. W., & Albrecht, S. 2009, Nature, 459, 543
Sozzetti, A. 2010, Highlights Astron., 15, 716
Stevenson, K. B., Harrington, J., Nymeyer, S., et al. 2010, Nature, 464, 1161
Swain, M. R., Bouwman, J., Akeson, R. L., Lawler, S., & Beichman, C. A. 2008a, ApJ, 674, 482
Swain, M. R., Deroo, P., Griffith, C. A., et al. 2010, Nature, 463, 637
Swain, M. R., Tinetti, G., Vasisht, G., et al. 2009a, ApJ, 704, 1616
Swain, M. R., Vasisht, G., & Tinetti, G. 2008b, Nature, 452, 329
Swain, M. R., Vasisht, G., Tinetti, G., et al. 2009b, ApJ, 690, L114
Tashkun, S. A., & Perevalov, V. I. 2011, J. Quant. Spectrosc. Radiat. Transfer, 112, 1403
Tinetti, G., Deroo, P., Swain, M. R., et al. 2010a, ApJ, 712, L139
Tinetti, G., Liang, M.-C., Vidal-Madjar, A., et al. 2007a, ApJ, 654, L99
Tinetti, G., Meadows, V. S., Crisp, D., et al. 2005, Astrobiology, 5, 461
Tinetti, G., Meadows, V. S., Crisp, D., et al. 2006, Astrobiology, 6, 34
Tinetti, G., Swain, M. R., Deroo, P., et al. 2010b, Faraday Discuss., 147, 369
Tinetti, G., Tennyson, J., Griffith, C. A., & Waldmann, I. 2011a, Phil. Trans. R. Soc. A, in press
Tinetti, G., Vidal-Madjar, A., Liang, M.-C., et al. 2007b, Nature, 448, 169
Tinetti, G., et al. 2011b, Exp. Astron.
Waldmann, I. P., Drossart, P., Tinetti, G., et al. 2012, ApJ, 744, 35
Williams, P. K. G., Charbonneau, D., Cooper, C. S., Showman, A. P., & Fortney, J. J. 2006, ApJ, 649, 1020
Winn, J. N., Matthews, J. M., Dawson, R. I., et al. 2011, ApJ, 737, L18
Wright, E. L., Eisenhardt, P. R. M., Mainzer, A. K., et al. 2010, AJ, 140, 1868
Yurchenko, S. N., Barber, R. J., & Tennyson, J. 2011, MNRAS, 413, 1828